ACS APPLIED MATERIALS & INTERFACES

www.acsami.org Research Article

Optical Properties of $MoSe_2$ Monolayer Implanted with Ultra-Low-Energy Cr Ions

Minh N. Bui,* Stefan Rost, Manuel Auge, Lanqing Zhou, Christoph Friedrich, Stefan Blügel, Silvan Kretschmer, Arkady V. Krasheninnikov, Kenji Watanabe, Takashi Taniguchi, Hans C. Hofsäss, Detlev Grützmacher, and Beata E. Kardynal*

Cite This: ACS Appl. Mater. Interfaces 2023, 15, 35321−35331 Read Online

ACCESS | Metrics & More | Article Recommendations | Supporting Information

ABSTRACT: This paper explores the optical properties of an exfoliated $MoSe_2$ monolayer implanted with Cr^+ ions, accelerated to 25 eV. Photoluminescence of the implanted $MoSe_2$ reveals an emission line from Cr-related defects that is present only under weak electron doping. Unlike band-to-band transition, the Cr-introduced emission is characterized by nonzero activation energy, long lifetimes, and weak response to the magnetic field. To rationalize the experimental results and get insights into the atomic structure of the defects, we modeled the Cr-ion irradiation process using ab initio molecular dynamics simulations followed by the electronic structure calculations of the system with defects. The experimental and theoretical results suggest that the recombination of electrons on the acceptors, which could be introduced by the Cr implantation-induced defects, with the valence band holes is the most likely origin of the low-energy emission. Our results demonstrate the potential of low-energy ion implantation as a tool to tailor the properties of two-dimensional (2D) materials by doping.

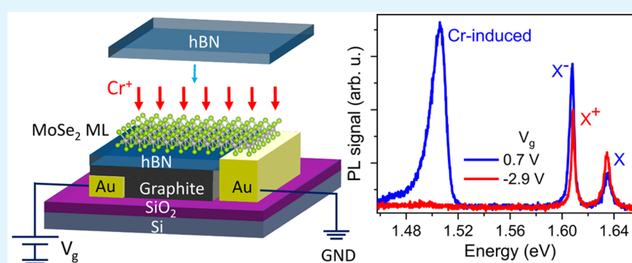

KEYWORDS: *transition-metal dichalcogenide monolayer, ultra-low-energy ion implantation, $MoSe_2$, van der Waals heterostructure, photoluminescence, molecular dynamics, density functional theory*

1. INTRODUCTION

The properties of semiconductors, especially atomically thin monolayer (ML) semiconductors, depend strongly on the types and densities of defects in their crystal lattices. The most technologically relevant defects are dopants, i.e., foreign atoms in substitutional positions in the crystal lattice. Shallow dopants introduce free electrons or holes into the conduction or valence band and thus change the semiconductor conductivity. As such, they facilitate the fabrication of p−n junctions, which underpins most active optoelectronic devices.

Doping with transition-metal atoms has been shown to introduce ferromagnetic order in p-doped semiconductors.[1] Impurity atoms can also trap electrons or holes or bind excitons. Radiative recombination involving such states can be detected as sub-band-gap photoluminescence (PL). Single foreign atom that bind excitons have been explored for single photon sources.[2] Alternatively, if the dopant atom has a functionality of a spin qubit, the bound excitons provide an optical readout of its state.[3,4] The binding of excitons to the dopant atoms depends not only on electron and hole masses but also on the dielectric constant of the semiconductors. Because of that, excitonic effects in bulk semiconductors are only observed at cryogenic temperatures. Foreign atoms can also act as color centers in semiconductors and insulators. Spin qubits based on the color centers have been realized in diamond[5,6] or SiC.[7,8]

In two-dimensional (2D) semiconducting transition-metal dichalcogenides (TMDs), which feature weak electrostatic screening, substitutional atoms tend to introduce deep levels in the band gaps.[9] While excitons have considerable binding energies, they are predicted to be very weakly bound to individual doping atoms.[10] Optical transitions involving defect states have been observed,[11] with defects identified as vacancies.[11−14] The transition responsible for the PL was found to occur between the hybridized defect states and 2D lattice electronic states.

Among several methods of doping bulk semiconductors, ion implantation offers the highest flexibility in choosing implanted elements. Ion energies of tens of keV are used for implantation since functional layers can be even a hundred nanometers below the surface. High-energy ion implantation has been used

Received: April 14, 2023
Accepted: June 23, 2023
Published: July 11, 2023

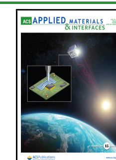

ACS Publications
© 2023 The Authors. Published by American Chemical Society

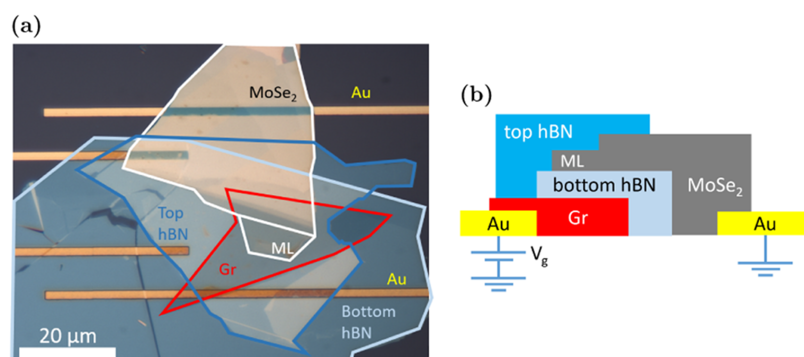

Figure 1. Cr-implanted $MoSe_2$ ML with hBN encapsulation and graphite backgate. (a) Micrograph of the finished device. The ML part of the exfoliated $MoSe_2$ flake is encapsulated between two thin hBN flakes. The few-layer graphite backgate and the thick part of $MoSe_2$ flake make contacts with the two Ti/Au lines to the right. (b) Schematic diagram of the device cross section. Backgate voltage V_g can be applied to the graphite backgate via the Au contact, while the $MoSe_2$ flake is grounded via the other Au contact.

to modify 2D materials,[15−17] but its efficiency is low in this case, as most atoms go through the 2D target.[18] Moreover, the ions penetrating through the ML can cause undesirable effects, e.g., trapped charges in the substrate. Implantation into 2D materials has the highest implantation efficiency with ion energies in the range of tens of eV. At these energies, the implantation efficiency and threshold energy depend on the ions' mass and also chemical properties.[19] Ultra-low-energy ion implantation[20,21] has recently been demonstrated to be efficient in doping graphene using 40 eV Mn ions[22,23] or in Se ion implantation into MoS_2 with an ion energy of 20 eV.[24,25] The ratio of the replaced S atoms with Se in the top sublattice was sufficient to form a Janus compound $MoS_{2-2x}Se_{2x}$ as indicated by Raman spectroscopy and the transmission electron microscopy imaging.

Here, we study the optical properties of molybdenum diselenide ($MoSe_2$) ML implanted with 25 eV $^{52}Cr^+$ ions. Sub-band-gap defect-induced PL emission was observed only at the low n-doping level and with saturation behavior, characteristic of defects with low density. Ab initio molecular dynamics (MD) simulations of the implantation process were performed, and possible configurations of the Cr atoms in the $MoSe_2$ ML lattice were outlined to understand the atomic structure of the implanted MLs. The optical properties of the $MoSe_2$ ML with such defects were calculated using density functional theory (DFT). The most probable defect configurations were identified by combining experimental data and theoretical calculations.

2. RESULTS

2.1. Sample Preparation and Ion Implantation. A sample for ion implantation was prepared by mechanical exfoliation of the $MoSe_2$, graphite (Gr), and hexagonal boron nitride (hBN) flakes and their sequential transfer onto the Si/SiO_2 substrate with pre-patterned Ti/Au contacts. The use of the dry viscoelastic transfer technique[26] ensured that the surface of the ML was sufficiently clean for the implantation. The $MoSe_2$ ML has to be grounded during the implantation. An electric contact to the ML was provided by placing the multilayer part of the exfoliated $MoSe_2$ flake on a Ti/Au metal contact. The ML was placed atop a graphite gate connected to another Ti/Au contact. The ML was separated from the gate with an hBN flake. Once completed, the device was implanted with $^{52}Cr^+$ ions at 25 eV and a fluence of 3×10^{12} cm^{-2} (equivalent to 0.003 Cr per ML $MoSe_2$ unit cell, using the $MoSe_2$ ML in-plane lattice constant 3.32 Å[27]). The implantation was performed with the device heated to 220 °C. Following the implantation and initial characterization, another hBN flake was deposited on the ML $MoSe_2$ for full encapsulation, which protects the ML from interactions with the environment during the optical measurement and reduces the inhomogeneous broadening in the PL linewidth.[28] The device was annealed at 150 °C to improve the interface between the constituent layers.[28] The complete device is shown in Figure 1. More details are available in Section 5.

2.2. Optical Spectroscopy Data. Figure 2a shows PL spectra of weakly electron-doped pristine and Cr-implanted $MoSe_2$ MLs, measured at 10 K with the same laser power of 1 μW. Both spectra show similar features around the band-gap transitions, with an emission line from neutral excitons (X) and negative trions (X^-). The red shift of these transitions in the Cr-implanted sample (Figure 2a) is most likely due to a difference in the dielectric environment or strain between the samples. The level of implantation is too low to expect changes in the band gap.[29] Significant homogeneous broadening of the X line was determined by the Voigt function fitting. It resulted in the Lorentzian width of nearly 7 meV for the implanted sample, compared to about 2 meV for the pristine sample, suggesting a much shorter lifetime of the former. The most significant difference between the samples is a broad emission at around 1.51 eV, which we label D.

The relative intensity of the D peak compared to X^- and X depends on the excitation power P (Figure 2b). It is the most intense line at low laser excitation powers ($P < 1$ μW) but saturates as the laser power increases, while X^- and X continue to grow linearly. The saturating behavior of the D intensity, shown in Figure 2c, can be expressed phenomenologically as

$$I \propto \frac{P}{P + P_{sat}} \quad (1)$$

with saturation power $P_{sat} \approx 10$ μW. The saturating behavior is expected when the exciton generation rate exceeds the recombination rate of the states responsible for D. The saturation threshold depends on the density of states and the lifetime of the recombining carriers.[11,13] The low threshold for D is consistent with the low implantation level. The lifetime of carriers was measured from time-resolved PL. The decay of the population of the excited states contributing to the D peak after a pulsed excitation can be seen in Figure 2d. As can be expected from measuring an ensemble of emitters, the decay is

https://doi.org/10.1021/acsami.3c05366
ACS Appl. Mater. Interfaces 2023, 15, 35321−35331

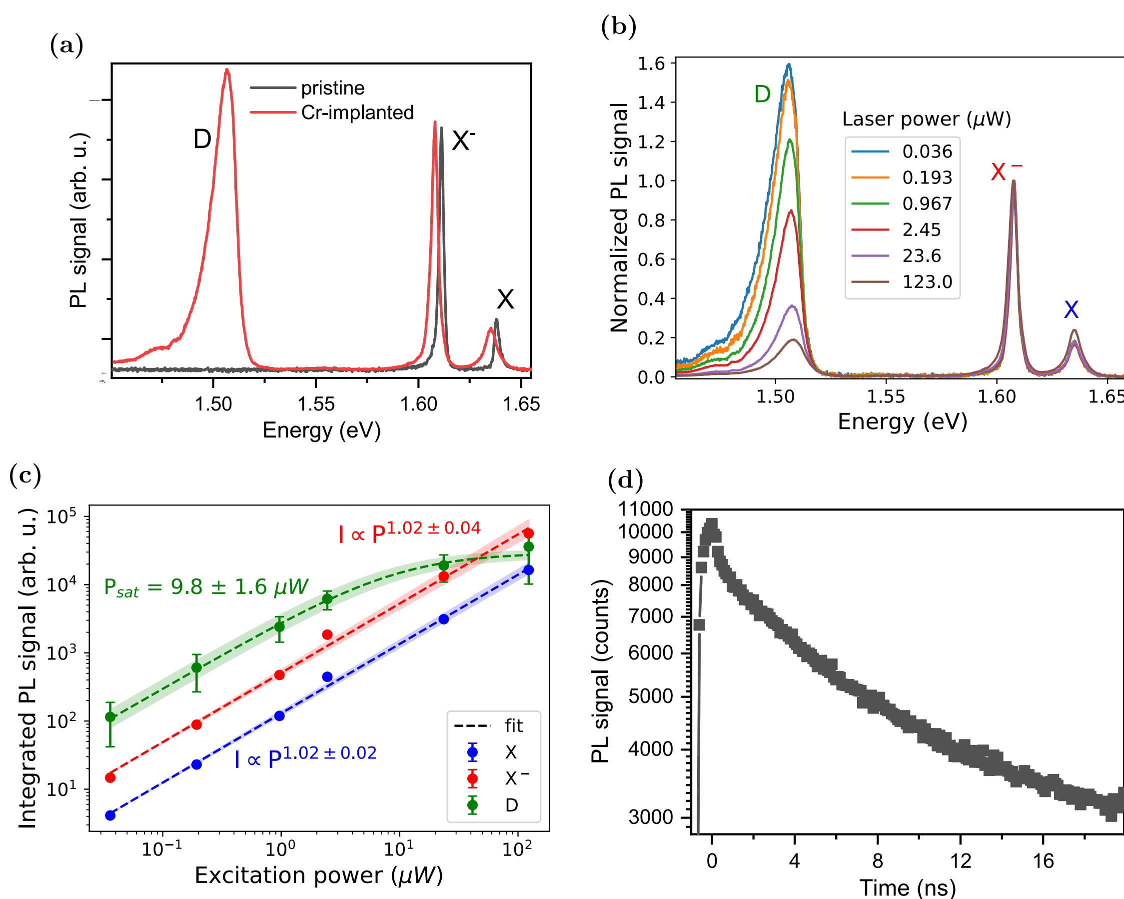

Figure 2. PL of Cr-implanted $MoSe_2$ ML at 10 K. (a) PL spectra of Cr-implanted $MoSe_2$ ML (red curve) at low n-doping (V_g = 0.8 V), plotted with that of pristine $MoSe_2$ ML (black). In addition to the X^- and X from $MoSe_2$ ML, the Cr-implanted sample also shows the broad D peak at around 1.51 eV. (b) PL spectra of Cr-implanted ML under laser power ranging from 36 nW to 123 μW. Spectra are normalized to X^-. Here, the sample is slightly n-doped at V_g = 0.8 V. (c) Power dependence of PL. Best-fit lines (dashed), with their standard deviations (shaded region around the lines), are plotted together with the extracted intensity from PL spectra (dots). Unless explicitly shown, the error bars are smaller than the size of the data points. X^- and X are fitted with power law $I \propto P^{\alpha}$, and D is fitted with the saturation curve described by eq 1. (d) Time-resolved PL of Cr-implanted $MoSe_2$. $1/e$ time is around 14 ns.

not a single exponential. The very fast initial decay of population by about 10%, which is faster than the time resolution of the experiment, is followed by a slower decay with the $1/e$ decay time of around 14 ns. These decay times are 2−3 orders of magnitude longer than the lifetime of free excitons in $MoSe_2$ MLs[30,31] and one order of magnitude longer than that from the isolated, confined excitons,[32] pointing to a low oscillator strength of the emitters.

The doping-dependent PL from neutral and charged excitons shown in Figure 3a is typical of $MoSe_2$ MLs. When increasing the gate voltage, the D emission only emerges after the signal from the positive trion, X^+, entirely disappears. It reaches the maximum intensity around 1 V; the gate voltage of the transition between X and X^- dominated spectra. The blueshift of the D emission at higher gate voltage is likely to be due to the energy renormalization due to the screening by the free charges in the ML. Similar behavior for defect peaks was observed by others.[33] The D line weakens strongly as the X^- line intensifies with a further gate voltage increase. This behavior suggests a competition between the exciton capture at the defect state and the formation of an X^-. This scenario is supported by the PL excitation (PLE) spectroscopy measurement (Figure 3b), which shows that the intensity of the D emission is maximum when the excitation wavelength is resonant with the energy of X around 1.637 eV. The D emission was not excited with laser resonant with X^- (around 1.608 eV) even though the PL spectrum, measured at the same

https://doi.org/10.1021/acsami.3c05366
ACS Appl. Mater. Interfaces 2023, 15, 35321−35331

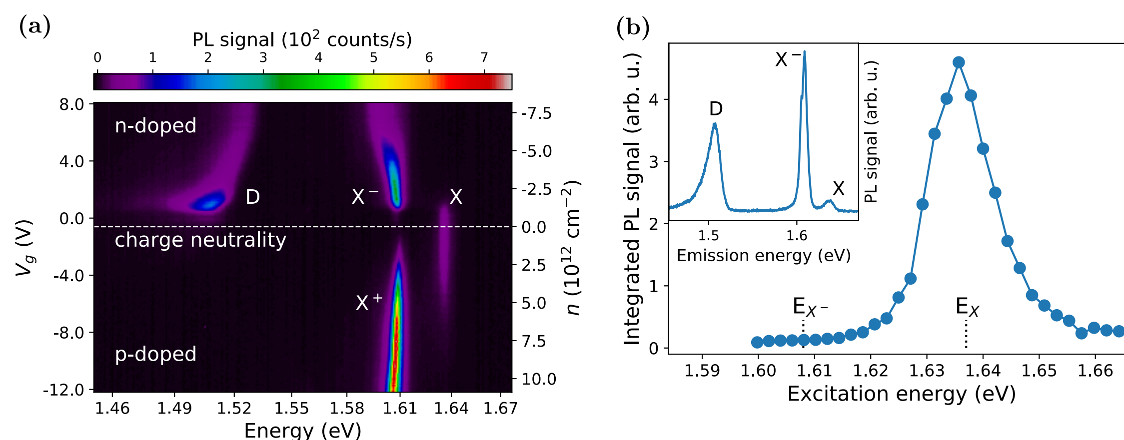

Figure 3. Doping level and excitation energy dependencies of PL. (a) Gate-dependent PL, where the backgate voltage V_g was varied from −12 to 8 V to tune the doping level in the ML from p- via neutral to n-doping. The carrier concentration n is calculated using the simple parallel plate capacitor model (more details in the Supporting Note 7). (b) PLE of the D peak, taken at V_g = 0.7 V. The D peak intensity was integrated around its PL emission energy between 1.48 and 1.52 eV. Inset: PL spectrum under a 688 nm (1.80 eV) excitation under the gate voltage as applied for the PLE measurements.

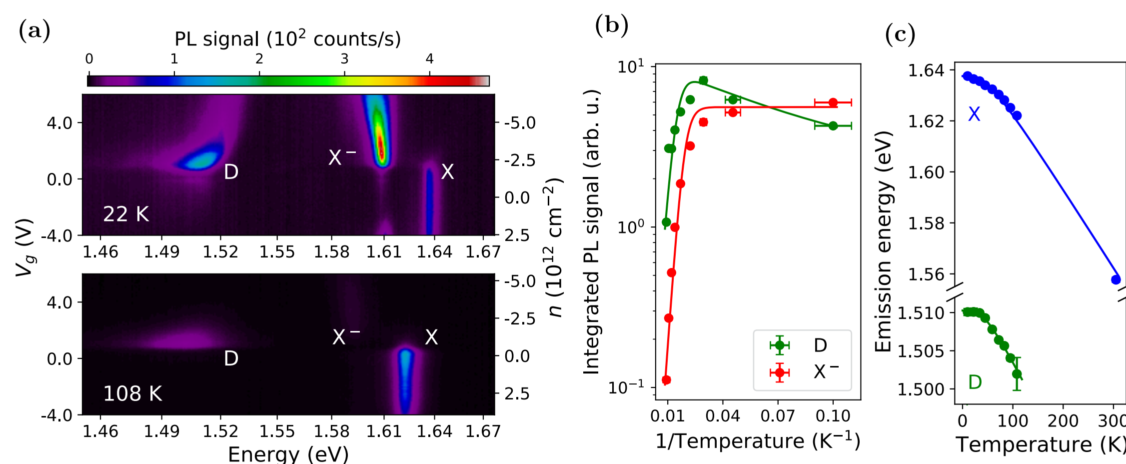

Figure 4. Temperature dependence of PL emission. (a) Gate voltage-dependent PL at 22 and 108 K. (b) Arrhenius plot of X⁻ and D (symbols). At each temperature, the two peaks' integrated intensities were acquired at the doping levels, where each emission is the brightest. The intensities were then normalized to that of X (at the voltage where X is most intense). The best fit lines were according to eqs 2 and 3. (c) The temperature-dependent band gap of X and D (symbols). The best-fit line was according to eq 4.

doping level, clearly shows that the ML is doped with electrons (X⁻ emission is the strongest PL signal).

Figure 4a compares gate-dependent PL at 22 and 108 K. While X⁻ emission is the most intense line in the spectra at the lower temperature, it is very weak at the higher temperature. X becomes the strongest line, but D diminished less than X⁻ and remains up to room temperature (Supporting Figure S4b). We trace the change of the PL signal counts from X⁻ and D, both normalized to X signal counts, on the Arrhenius plot shown in Figure 4b. X⁻ dissociates into higher-energy X and an electron at a higher temperature. Its intensity can be fitted with the standard Arrhenius formula[34]

$$I(T) = \frac{I(0)}{1 + A\exp\left(\frac{-E_a}{k_B T}\right)} \quad (2)$$

where $I(0)$ is the PL intensity at temperature 0 K, A is a proportionality constant, E_a is the activation energy for the dissociation of X⁻, and k_B is the Boltzmann constant. Fitting the formula to the data gives $E_a \approx 32 \pm 5$ meV, which is expected for a binding energy of the trion.[10,35] The D emission intensity first increased with temperature up to around 34 K before diminishing. To account for this initial increase in intensity, we assume that the trapping of carriers that recombine requires overcoming the activation energy. We use a modified multilevel model for the temperature dependence of the D intensity[34]

$$I(T) = I(0)\frac{1 + A_1\exp\left(\frac{-E_{a1}}{k_B T}\right)}{1 + A_2\exp\left(\frac{-E_{a2}}{k_B T}\right)} \quad (3)$$

where A_1 and A_2 are the proportionality constants, and E_{a1} and E_{a2} are the activation energies for trapping and detrapping of carriers, respectively. Fitting of the D peak yields $E_{a1} \approx 1.2 \pm 0.8$ meV and $E_{a2} \approx 30 \pm 7$ meV.

Temperature affects not only the intensity but also the D emission energy. The temperature-dependent energy shift of X and D lines can be described by the modified Varshni relation[13,36] as

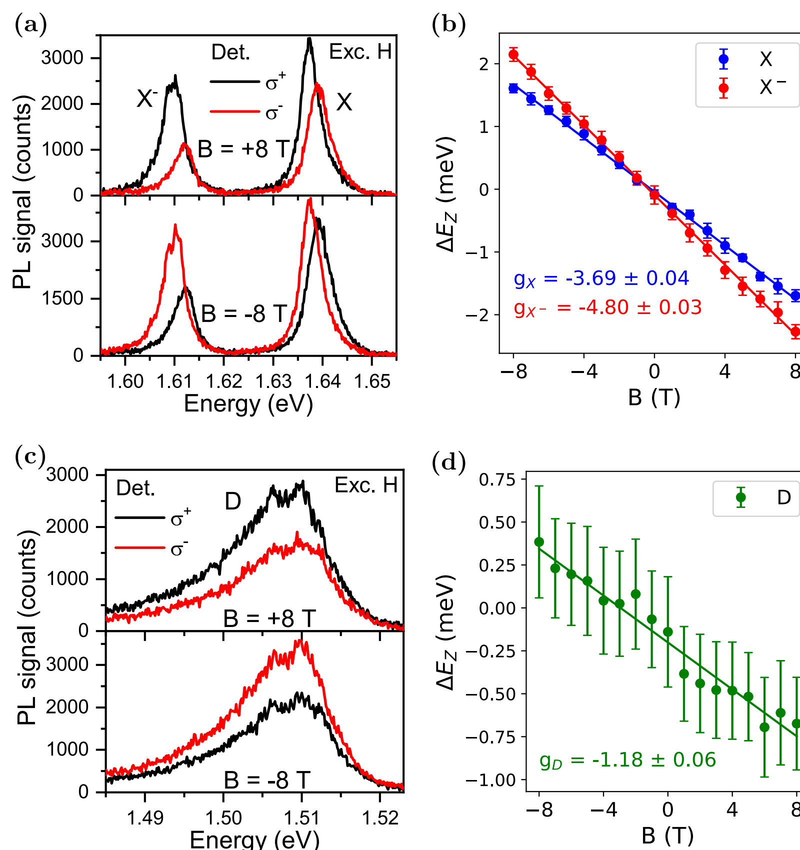

Figure 5. Magneto-PL measurement of Cr-implanted $MoSe_2$ ML at 1.8 K. PL spectra acquired with out-of-plane magnetic field B (varying between −8 and 8 T) applied to the sample and excited with an H-polarized laser. The detection is set to measure either σ^+ (black) or σ^- (red) polarization states. The figure shows the polarization-resolved PL spectra of (a) X and X⁻, (c) D, with their Zeeman splitting ΔE_Z shown in (b, d). The splitting was calculated from the peak positions (extracted from fitting Voigt functions to the PL spectra), with the error bars representing the propagated standard deviation of the fit procedure. The Zeeman splitting of the three emissions reveals expected g-factors around −4 for X and X⁻, only around −1.18 for D.

$$E_g(T) = E_g(0) - S\langle\hbar\omega\rangle\left[\coth\frac{\langle\hbar\omega\rangle}{2k_BT} - 1\right] \quad (4)$$

where $E_g(0)$ is the emission energy at 0 K, S is the electron−phonon coupling, and $\langle\hbar\omega\rangle$ is the average phonon energy. Fitting gives $\langle\hbar\omega\rangle$ = 11.1 ± 1.3 meV and S = 1.82 ± 0.14 for X, similar to the reported values ($\langle\hbar\omega\rangle \approx$ 12−20 meV, $S \approx$ 2.[37−39]). For the D emission, the fitted $\langle\hbar\omega\rangle$ and S are 10.7 ± 1.5 and 0.79 ± 0.09 meV, respectively. A smaller S constant compared to excitonic lines has been reported for vacancy-induced PL emissions from TMD MLs[13,14,40] and explained as a result of the defect being decoupled from the conduction band, which varies with the temperature. A similar scenario is also likely to be the case in our sample.

To gain further insight, we measured the PL emission from the sample under the out-of-plane magnetic field B varying from −8 to 8 T. Figure 5a shows the splitting of X and X⁻ spectra in two circular polarization detection states under the applied B-field. The valley splitting, caused by the Zeeman effect[41,42] and defined as

$$\Delta E_Z = E_{\sigma^+} - E_{\sigma^-} = g\mu_B B \quad (5)$$

(where E_{σ^+} and E_{σ^-} are the emission energy in the detected circular polarization basis σ^+ and σ^-, respectively, g is the Landé g-factor, μ_B is the Bohr magneton) changes linearly with the applied magnetic field (Figure 5b). The g-factors derived from the data are −3.69 ± 0.04 and −4.80 ± 0.03 for X and X⁻, respectively. The g-factor value for X is close to the ones from the previous experimental work,[28,41−45] which are between −3.8 and −4.3 and well within the expected range from −3.22 to −3.82 predicted by recent ab initio calculations.[46,47] The g-factor for X⁻ is slightly higher than for X but similar to the values observed for samples under higher doping level.[43−45] On the other hand, the D emission shows little change with the magnetic field (Figure 5c). Comparing the energy of photons from the D peak in both circular polarization gives a g-factor of about −1.18 ± 0.06. The peak position was determined by fitting the data with three Voigt functions and then taking the maximum of the fitted line. The uncertainty here is high, partly owing to the D peak's large width.

2.3. First-Principles Molecular Dynamics Simulation of Cr-Ion Implantation into $MoSe_2$ ML.

To get insights into the defect formation process and types of defects that can appear upon impacts of energetic Cr ions, we carried out DFT MD simulations, as described below. The atomic structure of a free-standing $MoSe_2$ rectangular slab containing 90 atoms was fully optimized; then, a Cr atom was placed 6 Å above its surface (Figure 6a) and a kinetic energy of 25 eV was assigned to the atom. Normal incidence was simulated; that is, the initial velocity vector of the projectile was oriented perpendicular to the surface of the ML. The projectile was assumed to be a neutral atom, as at such low energies and low

https://doi.org/10.1021/acsami.3c05366
ACS Appl. Mater. Interfaces 2023, 15, 35321−35331

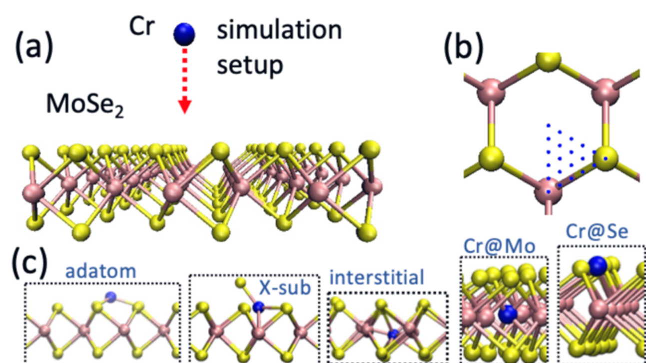

Figure 6. First-principles MD simulation of the ion implantation process into ML $MoSe_2$. (a) The setup for simulations of ion impacts. (b) Impact sites used in the simulation. (c) Atomic structures of the defects likely to appear upon impacts of energetic Cr ions.

charge states, its neutralization must occur well before it reaches the surface. We note that DFT MD on the Born–Oppenheimer surface cannot describe the evolution of charge transfer anyway, and the Ehrenfest dynamics[48,49] should be used. 21 impact points were selected in the irreducible area of the primitive cell of $MoSe_2$ (Figure 6b), and the outcomes of the simulations were averaged with the corresponding weights. The MD runs continued until the kinetic energy brought up by the projectile was distributed over the whole supercell (normally after a few picoseconds); then, the system's temperature was quenched to zero, and the atomic structure was analyzed. Although the effects of substrate on defect generation in a 2D system can be significant for ions with much higher (keV range) energies,[50−52] the role of the substrate should be minimal for impacts of 25 eV Cr ions onto $MoSe_2$, so that a free-standing slab was simulated. Spin-polarized calculations were carried out. Although computationally more efficient non-spin-polarized method with a correction for isolated atom polarization energies can be used to simulate irradiation effects,[19] the account for spin effects is particularly important for Cr, as it is magnetic, which affects the energetics of defect configurations.

Figure 6c shows the most common atomic configurations that appear after Cr atom impacts. These are Cr adatoms, X-sub configuration (Cr at Se sites with a Se adatom[53]), interstitials (the Cr atom between Mo atoms), and substitutional defects in Mo and Se sites, which are Cr@Mo and Cr@Se, respectively. Table 1 lists the probabilities for the defects to appear. Ion irradiation also gives rise to the sputtering of Se atoms, that is, the formation of Se vacancies (V_{Se}), but these events were not so common.

Table 1. Results of DFT MD Simulations of a 25 eV Cr-Ion Irradiation on a Single-Layer $MoSe_2$[a]

	p	E_f [eV]
adatom	0.16	−0.85
X-sub	0.41	−0.76
interstitial	0.08	−0.25
Cr@Mo	0.21	3.03
Cr@Se	0.04	2.57
V_{Se}	0.01	5.41
passed through	0.09	0.00

[a]The probabilities p of likely defect configurations to appear along with the formation energies E_f of these configurations are listed.

According to the DFT MD simulations, the most probable defects that appear upon 25 eV Cr-ion irradiation are Cr adatoms, Cr@Mo, and X-sub defects. The Cr atoms that pass through the $MoSe_2$ sheet will likely form adatoms attached to the bottom of $MoSe_2$. Self-annealing of defects at finite temperatures at which irradiation was carried out in the experiment can affect their concentrations in the implanted samples. To get insight into the possible evolution of defects, we assessed the defect formation energies E_f, as done previously.[53] For adatoms, interstitials, and X-sub defects, E_f was calculated as the energy difference between the system with the Cr atom and the pristine system plus isolated Cr atom. For the Cr@Mo, Cr@Se, and V_{Se} configurations, the energies of isolated Mo and Se atoms were also taken as a reference. We note that the listed defect formation energies for the Cr@Mo, Cr@Se, and V_{Se} cannot be used to assess the equilibrium concentrations of these defects, as the chemical potentials were chosen to match isolated, that is, sputtered, atoms. This can be done, though, if the chemical potentials of the displaced Se and Mo atoms are chosen in such a way that they reflect the actual experimental conditions that the potential can be anywhere between the values corresponding to the Se- or Mo-rich limits. This would result in lower formation energies, as the sputtered atoms would be incorporated into the lattice. It can also be assumed that the displaced Se atoms form Se clusters at the surface, which would give rise to the lowering of Cr@Se defect energies.

As evident from Table 1, E_f for adatoms is lower than for the interstitials, so that at finite temperatures, the interstitials will most likely be "pushed away" from the Mo plane and form adatoms. We note that this result was obtained for a relatively small 90-atom supercell, and in the larger system, the difference between these energies is smaller, as reported earlier.[53] Nevertheless, even for equal formation energies at zero temperature, with an account for the entropic term in the Gibbs energy, the probabilities for the adatoms should be higher due to a larger configurational space. Some X-sub defects may also be converted to Cr@Se configurations, especially in the Mo-rich limit, when Se vacancies are present, but the energetics of this process naturally depends on the experimental conditions, that is, the choice of Se chemical potential. The Cr@Se defects can also appear due to the adsorption of Cr atoms on Se vacancies, as this is energetically favorable due to the saturation of dangling bonds. Thus, one can expect that the most prolific defects in the samples are Cr adatoms (or Cr clusters on top of $MoSe_2$), X-sub, as well as Cr@Mo and Cr@Se substitutional configurations.

2.4. DFT Calculations of Optical Properties. To investigate if Cr defects introduce states in the band gap of the $MoSe_2$ ML that are optically active, we have simulated optical absorption spectra for $MoSe_2$ with Cr defects in various positions. The simulations are based on a 5×5 supercell. Each supercell hosts one Cr defect. The unfolded band structures are shown in the Supporting Figure S5. All defects give rise to states in the band gap. The absorption spectrum $\mathrm{Im}[\varepsilon(\omega)]$ with the energy-dependent macroscopic dielectric function $\varepsilon(\omega)$ has been calculated within the random-phase approximation in the limit $\mathbf{k} \rightarrow \mathbf{0}$. Optical matrix elements and local-field effects are taken into account. It should be pointed out that self-energy corrections (such as GW) or electron–hole interactions (as described by the Bethe–Salpeter equation) are neglected. Self-energy corrections and electron–hole interactions are known to have a partially compensating effect on

https://doi.org/10.1021/acsami.3c05366
ACS Appl. Mater. Interfaces 2023, 15, 35321−35331

the band gap:[54] while the former tends to increase the band gap, the electron−hole interactions make the optical band gap smaller. Due to this compensating effect, the present theoretical results can be seen as approximate spectra specifically showing the impact of the defects. However, quantitative differences between theory and experiment should be expected due to the neglect of many-body effects and also due to the difference in the dielectric environment. The theoretical spectra are shown in Figure 7. Absorption below the band gap (around 1.6 eV) is present for all defects and originates from transitions involving the defect states.

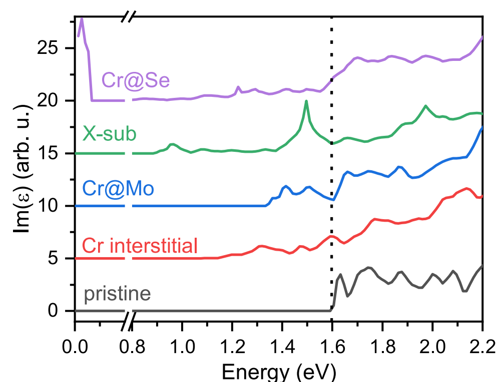

Figure 7. Comparison of calculated absorption functions for pristine $MoSe_2$ ML (black line) and $MoSe_2$ ML with Cr in various positions of the crystal structure: Cr at the interstitial position (red), Cr at the Mo position (Cr@Mo—blue), Cr at the Se position with additional Se adatom (X-sub, green), and Cr at the Se position (Cr@Se, purple). Spectra are offset vertically for clarity. The vertical dotted line at about 1.6 eV marks the calculated band gap of pristine $MoSe_2$ ML.

There is an optical transition for X-sub at 1.5 eV, which is in the same energy range of the D emission from the PL spectra between the valence band and an acceptor state of X-sub. This state results from the coupling of the conduction band at the *K*-point with the Cr defect state. The energy of this transition is similar to that of the $MoSe_2$ ML with a vacancy.[55−58]

The weak transition involving a deep acceptor state at 0.9 eV is outside the spectral range of our experiments. We note that the coupling between the conduction band and the defect state shifts the conduction band minimum from *K* toward the Γ point (Supporting Figure S5). However, the resulting suppression of PL would not be visible in the experiment due to the low density of defects and only the local opening of the band gap.

Well-defined spin-degenerate acceptor levels are also introduced by Cr substituting the Mo atom in the lattice (Cr@Mo). Optical transitions from this defect state into the valence band states can be seen in Figure 7 in the range between 1.4 and 1.5 eV, which is also in a similar energy range to the D peak PL emission. The band-to-band transition is shifted to higher energy compared to the pristine $MoSe_2$ ML because of the coupling between the conduction band and the defect state. However, similar to the X-sub configuration discussed above, it is unlikely to observe this blueshift in the PL spectra due to the low defect density.

The coupling of the defect and conduction band results in a gradual increase of the above-band-gap absorption for Cr substitution into the Se site (Cr@Se). This defect type also introduces a donor state at the Fermi level and two single-spin, deep defect levels. The signal from the donor state merges with the band-to-band absorption. Otherwise, the Cr defect at the Se site hardly affects the $MoSe_2$ band structure. Several weak optical transitions are present at a large range of energies (down to 500 meV below the band gap).

Interstitial Cr introduces several deep defect levels in the band gap, and again the highest state couples to the conduction band shifting the conduction band minimum to the Λ point. The absorption spectrum does not contain discrete absorption lines but a gradually increasing absorption from 1.2 eV.

3. DISCUSSION

Radiative recombination of an electron (e^-) bound to a defect state with the valence band hole (h^+) can explain the measured PL. Considering that our DFT calculations do not show donor states at high enough energy, the electron here is likely to occupy an acceptor. In this scenario, an exciton bound to a negatively charged acceptor (A^-X) dissociates into A^-h^+ and a free electron in the conduction band. Following radiative recombination, A^-h^+ becomes neutral acceptor A^0. Theoretical modeling of A^-X indicated a binding energy of only a few meV compared with the $A^0 + e^-$ state,[10] which is of the same order of magnitude as the activation energy of the D line determined from the Arrhenius plot. Among the potential defects identified by MD calculations, Cr@Mo, X-sub, and Cr@Se have nonzero matrix elements for optical transitions between acceptor states and valence band. Other configurations, e.g., interstitial Cr or Se vacancies, are unlikely to be present. Besides, neither would explain the data (see Figure 7 and Supporting Information Note 4).

The measured $1/e$ recombination time is longer than the lifetimes reported for band-to-band and localized state recombination in $MoSe_2$. Low oscillator strength of the transition can result from the spatial separation of electrons and holes, as for Cr@Se or X-sub. However, since this lifetime is longer than that of the spin dark states in WSe_2, which is only a few nanoseconds,[59] this transition could also be from a spin-forbidden state. Such a state would correspond to the charge configuration of A^0 for the Cr@Se defect in the absence of exchange interactions between electrons in the conduction band.

The *g*-factor of the D emission is negative but much smaller than those for X or X^-. With large *g*-factors for electrons in the valence band, it implies either a large *g*-factor for an electron on the acceptor level near the conduction band (e.g., in Cr@Mo or X-sub configuration) and valley-selective transitions or reduced *g*-factor of holes in the valence band. The latter could be caused by the hybridization of the valence band with the defect level as in the Cr@Se configuration. Further insight would require higher magnetic field measurements and theoretical input.

4. CONCLUSIONS

In conclusion, we demonstrated the ultra-low-energy ion implantation of Cr ions (at 25 eV) into a $MoSe_2$ ML. The implantation was performed with ions at 25 eV and an ion fluence of 3×10^{12} cm^{-2}; the resulting material retains high optical quality as evidenced by clear excitonic PL. Implanted Cr ions introduce an additional low-energy PL signal at around 1.51 eV visible at the onset of n-doping. Molecular dynamics calculations identified defects that can be generated by implantation. We found that Cr atoms can substitute for

https://doi.org/10.1021/acsami.3c05366
ACS Appl. Mater. Interfaces 2023, 15, 35321−35331

both Mo and Se atoms. In the latter case, the Cr atom is slightly more likely to bind an additional Se atom than not. The defects' stability, including interstitial Cr, depends on the post-implantation treatment and the final configuration of Se and Mo, which are not in the lattice. DFT calculations revealed that all of the probable defects introduce one or more defect states in the $MoSe_2$ band gap with nonzero matrix elements for optical transitions. It is impossible to identify with certainty which defect is the origin of the D line, Cr at the Se site with the Se adatom (X-sub), and perhaps Cr at Mo (Cr@Mo) seems to fit best with the measured data. Further experiments, for example, the implantation of Cr only into the Se sublattice or implantation through the hBN protective layer to avoid environmental changes, could be considered to distinguish between the cases.

More generally, this study shows that implantation of heavier elements into the metal sublattice of TMD MLs is possible without the visible loss of material quality as evidenced by the unchanged excitonic PL of gated $MoSe_2$. However, the implantation process is complex, and simulations of the possible outcomes are necessary to identify material systems of the desired properties. In the search for single photon emitting sites, it is also worth noting that upon implantation with a very low fluence, it should be possible to address individual Cr atoms at different lattice sites. Implantation of foreign atoms might be used to introduce catalytic sites in 2D materials or to add functionalization such as magnetism.

5. METHODS

5.1. Atomistic Simulation. We used DFT MD as implemented in the VASP code.[60,61] The Perdew–Burke–Ernzerhof (PBE) exchange and correlation functional was employed.[62] The evolution of the system was modeled using the microcanonical ensemble. A cutoff value of 300 eV was chosen for DFT MD, and sampling over the Brillouin zone was done using a $3 \times 3 \times 1$ k-point mesh. The time step was chosen to be 0.1 fs, which provided energy conservation better than 0.1 eV.

5.2. Band Structure and Absorption Spectral Calculation. Density functional theory (DFT) simulations were performed in supercells of 5×5 primitive unit cells. Each was constructed with lattice constants of a = 3.28 Å and c = 12.918 Å of the hexagonal lattice. An internal structure parameter of z = 0.125 was used. The defect systems were spatially relaxed using FLEUR[63,64] until the residual atomic forces had fallen below 5×10^{-2} eV/Å. The subsequent calculation of the macroscopic dielectric function in SPEX[65,66] is based on the random-phase approximation[67,68] and includes local-field effects. Calculations of 2D materials with 3D periodic boundary conditions are computationally expensive because the decoupling of neighboring layers in the z direction requires large supercells in this direction. In the case of 2D systems with defects, the computational cost grows considerably, particularly in the case of low defect concentrations, because suppressing the unwanted defect–defect coupling requires large supercells in the x and y directions. To facilitate the calculations of the dielectric function, we had to reduce the reciprocal cutoff radius from 4.1 to 3.6 Bohr^{-1} in the case of the X-sub defect system. However, this should not affect the form of the respective spectrum shown in Figure 7.

The band structures presented in the Supporting Information are made up of 320 $\mathbf{k}$ points along the unfolded high-symmetry path Γ–M–K–Γ. Here, "unfolded" means that the high-symmetry points refer to those of the defect-free $MoSe_2$ ML. The necessary unfolding of the band structures of the defect systems has been carried out with a new implementation[55] in the FLEUR code, adapting the technique described in ref 69 to the LAPW basis.[70] In this technique, a spectral weight is assigned to each state plotted in the band structure. The weight $w_n(\mathbf{k})$ for the n-th state at $\mathbf{k}$ of the unfolded path is given by

$$w_n(\mathbf{k}) = \sum_{\tilde{\mathbf{G}},\mathbf{G}'} C^*_{\mathbf{k}'n}(\tilde{\mathbf{G}}) \cdot C_{\mathbf{k}'n}(\mathbf{G}') \cdot S_{\tilde{\mathbf{G}}\mathbf{G}'}(\mathbf{k}') \quad (6)$$

where $\mathbf{k}' = \mathbf{k} + \mathbf{G}''$ with a suitable reciprocal lattice vector $\mathbf{G}''$ that folds $\mathbf{k}$ back into the (smaller) Brillouin zone of the defect system. The $\mathbf{G}'$ sum runs over the set of all reciprocal lattice vectors (of the defect system) at $\mathbf{k}'$, and the $\tilde{\mathbf{G}}$ sum runs over the set of reciprocal lattice vectors (of the pristine system) at $\mathbf{k}$. The latter is a subset of the former. The wave functions are represented in the LAPW basis $\{\chi_{\mathbf{kG}}(\mathbf{r})\}$ with coefficients $C_{\mathbf{k}n}(\mathbf{G})$ and overlap matrix $S_{\mathbf{GG}'}(\mathbf{k}) = \langle \chi_{\mathbf{kG}} | \chi_{\mathbf{kG}'} \rangle$.[55]

5.3. Sample Preparation. Si with 90 nm thick dry-thermally grown SiO_2 chips with 60 nm thick Ti/Au contacts (pre-patterned by electron beam lithography) were used as the substrate. Before flake transfer, the chips were cleaned in acetone and isopropanol (IPA) under bath sonication, blown dry with N_2, and treated with oxygen plasma (300 W, 200 sccm for 10 min). Few-layer graphite, $MoSe_2$ (from 2Dsemiconductors) MLs, and hBN (from Takashi Taniguchi and Kenji Watanabe) multilayers were mechanically exfoliated from bulk crystal using polydimethylsiloxane (PDMS) stamps (Gel-pak DGL X4 films) and transferred onto the substrate using the dry viscoelastic transfer process.[26] The process was performed in a N_2-filled glovebox. After transferring the graphite (5.5 nm thick) and bottom-hBN (20 nm thick) flakes, the sample was annealed in a H_2/Ar (1:10 ratio) atmosphere at 300 °C for 3 h to improve the top surface for the subsequent $MoSe_2$ ML transfer. After transferring the top-hBN (15 nm thick), the sample was annealed in low vacuum (5×10^{-3} mbar) at 150 °C for 2.5 h to improve interfaces in the vdW stack. Electrical contacts, provided by the Ti/Au lines, were made to the $MoSe_2$ flake and the graphite backgate. After each transfer, the heterostructure surface was checked with atomic force microscopy to ensure a sufficiently flat area in the stack and to obtain the flakes' thickness. $MoSe_2$ ML's quality was confirmed by Raman and PL spectroscopies at room temperature.[71]

5.4. Ion Implantation. Bronze tips were used to fix the sample on a holder, making contact with the sample's Au pads and, thus, the ML. To remove volatile contamination from the sample, the sample chamber was then evacuated to 10^{-9} mbar for several hours. The sample was heated to 150 °C for 10 min to remove residual volatile adsorbates and then to 220 °C during the implantation. A foil was used as a feedstock to provide $^{52}Cr^+$ ions. After extraction, the ions are decelerated from 30 keV to 25 eV directly in front of the sample. Since the deceleration voltage is set relative to the potential of the source anode, this energy represents the upper limit, with a tail toward lower energies. The fluence of the ions was set to 3×10^{12} cm^{-2}. The fluence was verified by test implantations using the Rutherford backscatter spectrometry (more information in the Supporting Information Note 1). A detailed description of the source and the implantation system can be found in the references.[20,21]

5.5. Optical Measurements. PL spectroscopy was performed at 10 K (unless otherwise specified) in a He-cooled cold-finger cryostat (Cryoindustries) with a heating element (allowing a sample temperature range from 10 to 300 K). For PL measurements, the laser beam—688 nm (1.80 eV) from a Ti:Sa laser—is passed through a 680 ± 5 nm band-pass filter before being focused by an aspheric lens (NA = 0.47) into a spot of 1.6 μm in diameter on the sample. Unless otherwise specified, the laser power on the sample was at 1 μW for PL experiments. The PL signal is collected by the same lens and passed through a 700 nm low-pass filter before being focused by an achromatic doublet (NA = 0.24) through the entrance slit of a Czerny–Turner spectrometer, dispersed by a 600 l/mm grating onto a CCD camera. For gate dependence and temperature dependence PL, the laser power was kept at 1 μW. For PLE, the excitation power ranged from 2 to 5 μW, and the PL intensity is normalized to the power density for final data.

For time-resolved PL, the excitation was done using a pulsed laser at 660 nm (1.88 eV) with a 200 ps pulse length, a 2.5 MHz repetition

https://doi.org/10.1021/acsami.3c05366
ACS Appl. Mater. Interfaces 2023, 15, 35321–35331

rate, and a 2.8 μW average power. The PL signal is directed through an 800 nm (1.55 eV) low-pass filter on the detection path before entering an avalanche photodiode with a 30 ps time resolution. The histogram of the time difference between the laser pulses and PL emission was acquired with a time tagger.

The sample was mounted on an $x-y-z$ Attocube stage in a He flow cryostat (attoDRY2100) for magneto-optics measurement at temperature T = 1.8 K. A magnetic field up to ±8 T was applied perpendicularly to the sample (Faraday configuration). The excitation laser beam (688 nm, i.e., 1.80 eV at 4 μW) was passed through a 680 nm band-pass filter and a linear polarizer in an H-configuration. The laser was focused by an aspheric lens (NA = 0.47) into a spot of ≈1.6 μm in diameter on the sample. The emitted PL was collected with the same objective. It was passed through a combination of $\lambda/4$, $\lambda/2$ waveplates, and a linear polarizer set to pass the $\sigma^{\pm}$ polarized light. It was then propagated via a single-mode optical fiber toward the entrance slit of a Czerny−Turner spectrometer, where it was dispersed by a 600 l/mm grating onto a CCD camera. A long-pass filter (with a 700 nm band edge) was inserted between the fiber output and the spectrometer entrance to remove any remaining laser light.

■ ASSOCIATED CONTENT

Data Availability Statement

The data supporting the findings of this study are available within the paper and its Supporting Information files. Data are also available from the corresponding author upon reasonable request.

Supporting Information

The Supporting Information is available free of charge at https://pubs.acs.org/doi/10.1021/acsami.3c05366.

> Additional experimental details on the RBS measurement of Cr implantation on the test ta-C substrate; spatial PL maps of D, X, and X^-; polarization-resolved PL; Raman and PL spectroscopic studies of vacancies in $MoSe_2$ ML; MD simulation and TEM studies of Cr implantation on MoS_2 ML; unfolded band structure of Cr-implanted $MoSe_2$ ML with various defect configurations; and charge carrier density conversion from gate voltage (PDF)

■ AUTHOR INFORMATION

Corresponding Authors

Minh N. Bui − *Peter Grünberg Institute 9 (PGI-9), Forschungszentrum Jülich, 52425 Jülich, Germany; Department of Physics, RWTH Aachen University, 52074 Aachen, Germany;* orcid.org/0000-0003-4146-5026; Email: m.bui@fz-juelich.de

Beata E. Kardynał − *Peter Grünberg Institute 9 (PGI-9), Forschungszentrum Jülich, 52425 Jülich, Germany; Department of Physics, RWTH Aachen University, 52074 Aachen, Germany;* Email: b.kardynal@fz-juelich.de

Authors

Stefan Rost − *Peter Grünberg Institute 1 (PGI-1) and Institute for Advanced Simulation 1 (IAS-1), Forschungszentrum Jülich and JARA, 52425 Jülich, Germany; Department of Physics, RWTH Aachen University, 52074 Aachen, Germany*

Manuel Auge − *II. Institute of Physics, University of Göttingen, 37077 Göttingen, Germany*

Lanqing Zhou − *Peter Grünberg Institute 9 (PGI-9), Forschungszentrum Jülich, 52425 Jülich, Germany; Department of Physics, RWTH Aachen University, 52074 Aachen, Germany*

Christoph Friedrich − *II. Institute of Physics, University of Göttingen, 37077 Göttingen, Germany*

Stefan Blügel − *II. Institute of Physics, University of Göttingen, 37077 Göttingen, Germany; Department of Physics, RWTH Aachen University, 52074 Aachen, Germany;* orcid.org/0000-0001-9987-4733

Silvan Kretschmer − *Institute of Ion Beam Physics and Materials Research, Helmholtz-Zentrum Dresden-Rossendorf, 01328 Dresden, Germany;* orcid.org/0000-0002-5098-5763

Arkady V. Krasheninnikov − *Institute of Ion Beam Physics and Materials Research, Helmholtz-Zentrum Dresden-Rossendorf, 01328 Dresden, Germany; Department of Applied Physics, Aalto University School of Science, 00076 Aalto, Finland;* orcid.org/0000-0003-0074-7588

Kenji Watanabe − *Research Center for Functional Materials, National Institute for Materials Science, Tsukuba 305-0044, Japan;* orcid.org/0000-0003-3701-8119

Takashi Taniguchi − *International Center for Materials Nanoarchitectonics, National Institute for Materials Science, Tsukuba 305-0044, Japan;* orcid.org/0000-0002-1467-3105

Hans C. Hofsäss − *II. Institute of Physics, University of Göttingen, 37077 Göttingen, Germany*

Detlev Grützmacher − *Peter Grünberg Institute 9 (PGI-9), Forschungszentrum Jülich, 52425 Jülich, Germany*

Complete contact information is available at: https://pubs.acs.org/10.1021/acsami.3c05366

Author Contributions

B.E.K., H.C.H., and M.N.B. conceived and designed the experiments. S.K. and A.V.K. performed MD simulations. S.R., C.F., and S.B. performed DFT calculations for band structures and absorption spectra. T.T. and K.W. grew high-quality hBN crystals. L.Z. processed the Si/SiO_2 substrate with patterned markers and metal contacts. M.N.B. prepared the samples on the Si/SiO_2 substrate. M.A. and H.C.H. performed ion implantation. M.N.B. and L.Z. acquired and analyzed PL and Raman data. All authors discussed the results and contributed to the writing of this manuscript.

Funding

Volkswagen Foundation: "Integration of Molecular Components in Functional Macroscopic Systems" initiative, grant numbers 93425, 93427, and 93428. German Research Foundation (DFG): project KR 4866/8-1, and the collaborative research center "Chemistry of Synthetic 2D Materials" SFB-1415-417590517. Japan Society for the Promotion of Science (JSPS): Grants-in-Aid for Scientific Research (KAKENHI), grant numbers 19H05790 and 20H00354.

Notes

The authors declare no competing financial interest.
All scripts used to generate the results in this study are available from the corresponding author upon reasonable request.

■ ACKNOWLEDGMENTS

This project was supported by the "Integration of Molecular Components in Functional Macroscopic Systems" initiative of Volkswagen Foundation (grant numbers 93425, 93427, and 93428). The authors would like to thank the staff at the

Helmholtz Nano Facility[72] of Forschungszentrum Jülich for helping with substrate fabrication and Felix Junge (II. Institute of Physics, University of Göttingen, Göttingen, Germany) for organizing the RBS data, and the authors acknowledge the usage of VESTA software[73] for producing the graphics and the computing time granted through JARA-HPC on the supercomputer JURECA at Forschungszentrum Jülich. A.V.K. acknowledges funding from the German Research Foundation (DFG), project KR 4866/8-1, and the collaborative research center "Chemistry of Synthetic 2D Materials" SFB-1415-417590517. Generous grants of computer time from the Technical University of Dresden computing cluster (TAURUS) and the High Performance Computing Center (HLRS) in Stuttgart, Germany, are gratefully appreciated. K.W. and T.T. acknowledge support from the JSPS KAKENHI (grant numbers 19H05790 and 20H00354).

■ REFERENCES

(1) Dietl, T.; Ohno, H. Dilute Ferromagnetic Semiconductors: Physics and Spintronic Structures. *Rev. Mod. Phys.* **2014**, *86*, 187−251.

(2) Ikezawa, M.; Sakuma, Y.; Zhang, L.; Sone, Y.; Mori, T.; Hamano, T.; Watanabe, M.; Sakoda, K.; Masumoto, Y. Single-Photon Generation from a Nitrogen Impurity Center in GaAs. *Appl. Phys. Lett.* **2012**, *100*, No. 042106.

(3) Niaouris, V.; Durnev, M. V.; Linpeng, X.; Viitaniemi, M. L. K.; Zimmermann, C.; Vishnuradhan, A.; Kozuka, Y.; Kawasaki, M.; Fu, K.-M. C. Ensemble Spin Relaxation of Shallow Donor Qubits in ZnO. *Phys. Rev. B* **2022**, *105*, No. 195202.

(4) Vandersypen, L. M. K.; Bluhm, H.; Clarke, J. S.; Dzurak, A. S.; Ishihara, R.; Morello, A.; Reilly, D. J.; Schreiber, L. R.; Veldhorst, M. Interfacing Spin Qubits in Quantum Dots and Donors—Hot, Dense, and Coherent. *npj Quantum Inf.* **2017**, *3*, No. 34.

(5) Sekiguchi, Y.; Yasui, Y.; Tsurumoto, K.; Koga, Y.; Reyes, R.; Kosaka, H. Geometric Entanglement of a Photon and Spin Qubits in Diamond. *Commun. Phys.* **2021**, *4*, No. 264.

(6) Metsch, M. H.; Senkalla, K.; Tratzmiller, B.; Scheuer, J.; Kern, M.; Achard, J.; Tallaire, A.; Plenio, M. B.; Siyushev, P.; Jelezko, F. Initialization and Readout of Nuclear Spins via a Negatively Charged Silicon-Vacancy Center in Diamond. *Phys. Rev. Lett.* **2019**, *122*, No. 190503.

(7) Wolfowicz, G.; Anderson, C. P.; Diler, B.; Poluektov, O. G.; Heremans, F. J.; Awschalom, D. D. Vanadium Spin Qubits as Telecom Quantum Emitters in Silicon Carbide. *Sci. Adv.* **2020**, *6*, No. eaaz1192.

(8) Lohrmann, A.; Iwamoto, N.; Bodrog, Z.; Castelletto, S.; Ohshima, T.; Karle, T. J.; Gali, A.; Prawer, S.; McCallum, J. C.; Johnson, B. C. Single-Photon Emitting Diode in Silicon Carbide. *Nat. Commun.* **2015**, *6*, No. 7783.

(9) Ma, J.; Yu, Z. G.; Zhang, Y.-W. Tuning Deep Dopants to Shallow Ones in 2D Semiconductors by Substrate Screening: The Case of X_S (X = Cl, Br, I) in MoS_2. *Phys. Rev. B* **2017**, *95*, No. 165447.

(10) Mostaani, E.; Szyniszewski, M.; Price, C. H.; Maezono, R.; Danovich, M.; Hunt, R. J.; Drummond, N. D.; Fal'ko, V. I. Diffusion Quantum Monte Carlo Study of Excitonic Complexes in Two-Dimensional Transition-Metal Dichalcogenides. *Phys. Rev. B* **2017**, *96*, No. 075431.

(11) Rivera, P.; He, M.; Kim, B.; et al. Intrinsic Donor-Bound Excitons in Ultraclean Monolayer Semiconductors. *Nat. Commun.* **2021**, *12*, No. 871.

(12) Borghardt, S.; Tu, J.-S.; Taniguchi, T.; Watanabe, K.; Kardynał, B. E. Interplay of Excitonic Complexes in p-Doped WSe_2 Monolayers. *Phys. Rev. B* **2020**, *101*, No. 161402.

(13) Klein, J.; Lorke, M.; Florian, M.; et al. Site-Selectively Generated Photon Emitters in Monolayer MoS_2 via Local Helium Ion Irradiation. *Nat. Commun.* **2019**, *10*, No. 2755.

(14) Mitterreiter, E.; Schuler, B.; Micevic, A.; et al. The Role of Chalcogen Vacancies for Atomic Defect Emission in MoS_2. *Nat. Commun.* **2021**, *12*, No. 3822.

(15) Xu, K.; Zhao, Y.; Lin, Z.; Long, Y.; Wang, Y.; Chan, M.; Chai, Y. Doping of Two-Dimensional MoS_2 by High Energy Ion Implantation. *Semicond. Sci. Technol.* **2017**, *32*, No. 124002.

(16) Prucnal, S.; Hashemi, A.; Ghorbani-Asl, M.; Hübner, R.; Duan, J.; Wei, Y.; Sharma, D.; Zahn, D. R. T.; Ziegenrücker, R.; Kentsch, U.; Krasheninnikov, A. V.; Helm, M.; Zhou, S. Chlorine Doping of $MoSe_2$ Flakes by Ion Implantation. *Nanoscale* **2021**, *13*, 5834−5846.

(17) Jadwiszczak, J.; Maguire, P.; Cullen, C. P.; Duesberg, G. S.; Zhang, H. Doping Graphene with Substitutional Mn. *Beilstein J. Nanotechnol.* **2020**, *11*, 1329−1335.

(18) Krasheninnikov, A. V. Are Two-Dimensional Materials Radiation Tolerant? *Nanoscale Horiz.* **2020**, *5*, 1447−1452.

(19) Kretschmer, S.; Ghaderzadeh, S.; Facsko, S.; Krasheninnikov, A. V. Threshold Ion Energies for Creating Defects in 2D Materials from First-Principles Calculations: Chemical Interactions Are Important. *J. Phys. Chem. Lett.* **2022**, *13*, 514−519.

(20) Auge, M.; Junge, F.; Hofsäss, H. Laterally Controlled Ultra-low Energy Ion Implantation Using Electrostatic Masking. *Nucl. Instrum. Methods Phys. Res., Sect. B* **2022**, *512*, 96−101.

(21) Junge, F.; Auge, M.; Hofsäss, H. Sputter Hot Filament Hollow Cathode Ion Source and Its Application to Ultra-Low Energy Ion Implantation in 2D Materials. *Nucl. Instrum. Methods Phys. Res., Sect. B* **2022**, *510*, 63−68.

(22) Lin, P.-C.; Villarreal, R.; Achilli, S.; et al. Doping Graphene with Substitutional Mn. *ACS Nano* **2021**, *15*, 5449−5458.

(23) Lin, P.-C.; Villarreal, R.; Bana, H.; et al. Thermal Annealing of Graphene Implanted with Mn at Ultralow Energies: From Disordered and Contaminated to Nearly Pristine Graphene. *J. Phys. Chem. C* **2022**, *126*, 10494−10505.

(24) Bui, M. N.; Rost, S.; Auge, M.; et al. Low-energy Se Ion Implantation in MoS_2 Monolayers. *npj 2D Mater. Appl.* **2022**, *6*, No. 42.

(25) Bangert, U.; Stewart, A.; O'Connell, E.; Courtney, E.; Ramasse, Q.; Kepaptsoglou, D.; Hofsäss, H.; Amani, J.; Tu, J.-S.; Kardynal, B. Ion-beam Modification of 2-D Materials - Single Implant Atom Analysis via Annular Dark-Field Electron Microscopy. *Ultramicroscopy* **2017**, *176*, 31−36. 70th Birthday of Robert Sinclair and 65th Birthday of Nestor J. Zaluzec PICO 2017 — Fourth Conference on Frontiers of Aberration Corrected Electron Microscopy.

(26) Castellanos-Gomez, A.; Buscema, M.; Molenaar, R.; Singh, V.; Janssen, L.; van der Zant, H. S. J.; Steele, G. A. Deterministic Transfer of Two-Dimensional Materials by All-Dry Viscoelastic Stamping. *2D Mater.* **2014**, *1*, No. 011002.

(27) Kang, J.; Tongay, S.; Zhou, J.; Li, J.; Wu, J. Band Offsets and Heterostructures of Two-Dimensional Semiconductors. *Appl. Phys. Lett.* **2013**, *102*, No. 012111.

(28) Cadiz, F.; Courtade, E.; Robert, C.; et al. Excitonic Linewidth Approaching the Homogeneous Limit in MoS_2-Based van der Waals Heterostructures. *Phys. Rev. X* **2017**, *7*, No. 021026.

(29) Ho, C.-H.; Lai, X.-R. Effect of Cr on the Structure and Property of $Mo_{1-x}Cr_xSe_2$ ($0 \leq x \leq 0.2$) and Cr_2Se_{33}. *ACS Appl. Electron. Mater.* **2019**, *1*, 370−378.

(30) Fang, H. H.; Han, B.; Robert, C.; Semina, M. A.; Lagarde, D.; Courtade, E.; Taniguchi, T.; Watanabe, K.; Amand, T.; Urbaszek, B.; Glazov, M. M.; Marie, X. Control of the Exciton Radiative Lifetime in van der Waals Heterostructures. *Phys. Rev. Lett.* **2019**, *123*, No. 067401.

(31) Robert, C.; Lagarde, D.; Cadiz, F.; Wang, G.; Lassagne, B.; Amand, T.; Balocchi, A.; Renucci, P.; Tongay, S.; Urbaszek, B.; Marie, X. Exciton Radiative Lifetime in Transition Metal Dichalcogenide Monolayers. *Phys. Rev. B* **2016**, *93*, No. 205423.

(32) Yu, L.; Deng, M.; Zhang, J. L.; Borghardt, S.; Kardynal, B.; Vučković, J.; Heinz, T. F. Site-Controlled Quantum Emitters in Monolayer $MoSe_2$. *Nano Lett.* **2021**, *21*, 2376−2381.

(33) Hötger, A.; Klein, J.; et al. Gate-Switchable Arrays of Quantum Light Emitters in Contacted Monolayer MoS_2 van der Waals Heterodevices. *Nano Lett.* **2021**, *21*, 1040−1046.
(34) Shibata, H. Negative Thermal Quenching Curves in Photoluminescence of Solids. *Jpn. J. Appl. Phys.* **1998**, *37*, No. 550.
(35) Szyniszewski, M.; Mostaani, E.; Drummond, N. D.; Fal'ko, V. I. Binding Energies of Trions and Biexcitons in Two-Dimensional Semiconductors from Diffusion Quantum Monte Carlo Calculations. *Phys. Rev. B* **2017**, *95*, No. 081301.
(36) O'Donnell, K. P.; Chen, X. Temperature Dependence of Semiconductor Band Gaps. *Appl. Phys. Lett.* **1991**, *58*, 2924−2926.
(37) Li, X.; Puretzky, A. A.; Sang, X.; KC, S.; Tian, M.; Ceballos, F.; Mahjouri-Samani, M.; Wang, K.; Unocic, R. R.; Zhao, H.; Duscher, G.; Cooper, V. R.; Rouleau, C. M.; Geohegan, D. B.; Xiao, K. Suppression of Defects and Deep Levels Using Isoelectronic Tungsten Substitution in Monolayer $MoSe_2$. *Adv. Funct. Mater.* **2017**, *27*, No. 1603850.
(38) Choi, B. K.; Kim, M.; Jung, K.-H.; Kim, J.; Yu, K.-S.; Chang, Y. J. Temperature Dependence of Band Gap in $MoSe_2$ Grown by Molecular Beam Epitaxy. *Nanoscale Res. Lett.* **2017**, *12*, No. 492.
(39) Kioseoglou, G.; Hanbicki, A. T.; Currie, M.; Friedman, A. L.; Jonker, B. T. Optical Polarization and Intervalley Scattering in Single Layers of MoS_2 and $MoSe_2$. *Sci. Rep.* **2016**, *6*, No. 25041.
(40) Parto, K.; Azzam, S. I.; Banerjee, K.; Moody, G. Defect and Strain Engineering of Monolayer WSe_2 Enables Site-Controlled Single-Photon Emission up to 150 K. *Nat. Commun.* **2021**, *12*, No. 3585.
(41) Wang, G.; Bouet, L.; Glazov, M. M.; Amand, T.; Ivchenko, E. L.; Palleau, E.; Marie, X.; Urbaszek, B. Magneto-Optics in Transition Metal Diselenide Monolayers. *2D Mater.* **2015**, *2*, No. 034002.
(42) Koperski, M.; Molas, M. R.; Arora, A.; Nogajewski, K.; Bartos, M.; Wyzula, J.; Vaclavkova, D.; Kossacki, P.; Potemski, M. Orbital, Spin and Valley Contributions to Zeeman Splitting of Excitonic Resonances in $MoSe_2$, WSe_2 and WS_2 Monolayers. *2D Mater.* **2019**, *6*, No. 015001.
(43) Li, Y.; Ludwig, J.; Low, T.; Chernikov, A.; Cui, X.; Arefe, G.; Kim, Y. D.; van der Zande, A. M.; Rigosi, A.; Hill, H. M.; Kim, S. H.; Hone, J.; Li, Z.; Smirnov, D.; Heinz, T. F. Valley Splitting and Polarization by the Zeeman Effect in Monolayer $MoSe_2$. *Phys. Rev. Lett.* **2014**, *113*, No. 266804.
(44) MacNeill, D.; Heikes, C.; Mak, K. F.; Anderson, Z.; Kormányos, A.; Zólyomi, V.; Park, J.; Ralph, D. C. Breaking of Valley Degeneracy by Magnetic Field in Monolayer $MoSe_2$. *Phys. Rev. Lett.* **2015**, *114*, No. 037401.
(45) Back, P.; Sidler, M.; Cotlet, O.; Srivastava, A.; Takemura, N.; Kroner, M.; Imamoğlu, A. Giant Paramagnetism-Induced Valley Polarization of Electrons in Charge-Tunable Monolayer $MoSe_2$. *Phys. Rev. Lett.* **2017**, *118*, No. 237404.
(46) Deilmann, T.; Krüger, P.; Rohlfing, M. Ab Initio Studies of Exciton *g* Factors: Monolayer Transition Metal Dichalcogenides in Magnetic Fields. *Phys. Rev. Lett.* **2020**, *124*, No. 226402.
(47) Woźniak, T.; Faria, P. E., Junior; Seifert, G.; Chaves, A.; Kunstmann, J. Exciton *g* Factors of van der Waals Heterostructures from First-Principles Calculations. *Phys. Rev. B* **2020**, *101*, No. 235408.
(48) Gruber, E.; Wilhelm, R. A.; Pétuya, R.; et al. Ultrafast Electronic Response of Graphene to a Strong and Localized Electric Field. *Nat. Commun.* **2016**, *7*, No. 13948.
(49) Ojanperä, A.; Krasheninnikov, A. V.; Puska, M. Electronic Stopping Power from First-Principles Calculations with Account for Core Electron Excitations and Projectile Ionization. *Phys. Rev. B* **2014**, *89*, No. 035120.
(50) Kalbac, M.; Lehtinen, O.; Krasheninnikov, A. V.; Keinonen, J. Ion-Irradiation-Induced Defects in Isotopically-Labeled Two Layered Graphene: Enhanced In-Situ Annealing of the Damage. *Adv. Mater.* **2013**, *25*, 1004−1009.
(51) Kretschmer, S.; Maslov, M.; Ghaderzadeh, S.; Ghorbani-Asl, M.; Hlawacek, G.; Krasheninnikov, A. V. Supported Two-Dimensional Materials under Ion Irradiation: The Substrate Governs Defect Production. *ACS Appl. Mater. Interfaces* **2018**, *10*, 30827−30836.
(52) Standop, S.; Lehtinen, O.; Herbig, C.; Lewes-Malandrakis, G.; Craes, F.; Kotakoski, J.; Michely, T.; Krasheninnikov, A. V.; Busse, C. Ion Impacts on Graphene/Ir(111): Interface Channeling, Vacancy Funnels, and a Nanomesh. *Nano Lett.* **2013**, *13*, 1948−1955.
(53) Karthikeyan, J.; Komsa, H.-P.; Batzill, M.; Krasheninnikov, A. V. Which Transition Metal Atoms Can Be Embedded into Two-Dimensional Molybdenum Dichalcogenides and Add Magnetism? *Nano Lett.* **2019**, *19*, 4581−4587.
(54) Liu, G.-B.; Xiao, D.; Yao, Y.; Xu, X.; Yao, W. Electronic Structures and Theoretical Modelling of Two-Dimensional Group-VIB transition metal dichalcogenides. *Chem. Soc. Rev.* **2015**, *44*, 2643−2663.
(55) Rost, S. H. Computational Study of Structural and Optical Properties of Two-Dimensional Transition-Metal Dichalcogenides with Implanted Defects. Dissertation; RWTH Aachen University: Jülich, 2023.
(56) Iberi, V.; Liang, L.; Ievlev, A. V.; Stanford, M. G.; Lin, M.-W.; Li, X.; Mahjouri-Samani, M.; Jesse, S.; Sumpter, B. G.; Kalinin, S. V.; Joy, D. C.; Xiao, K.; Belianinov, A.; Ovchinnikova, O. S. Nanoforging Single Layer $MoSe_2$ Through Defect Engineering with Focused Helium Ion Beams. *Sci. Rep.* **2016**, *6*, No. 30481.
(57) Mahjouri-Samani, M.; Liang, L.; Oyedele, A.; et al. Tailoring Vacancies Far Beyond Intrinsic Levels Changes the Carrier Type and Optical Response in Monolayer $MoSe_{2-x}$ Crystals. *Nano Lett.* **2016**, *16*, 5213−5220.
(58) Shafqat, A.; Iqbal, T.; Majid, A. A DFT Study of Intrinsic Point Defects in Monolayer $MoSe_2$. *AIP Adv.* **2017**, *7*, No. 105306.
(59) Tang, Y.; Mak, K. F.; Shan, J. Long Valley Lifetime of Dark Excitons in Single-Layer WSe_2. *Nat. Commun.* **2019**, *10*, No. 4047.
(60) Kresse, G.; Hafner, J. Ab-Initio Molecular Dynamics for Liquid Metals. *Phys. Rev. B* **1993**, *47*, 558−561.
(61) Kresse, G.; Furthmüller, J. Efficiency of Ab-initio Total Energy Calculations for Metals and Semiconductors Using a Plane-Wave Basis Set. *Comput. Mater. Sci.* **1996**, *6*, 15−50.
(62) Perdew, J. P.; Burke, K.; Ernzerhof, M. Generalized Gradient Approximation Made Simple. *Phys. Rev. Lett.* **1996**, *77*, 3865−3868.
(63) The FLEUR project. https://www.flapw.de/.
(64) Wortmann, D. et al. FLEUR. Zenodo. 2023, https://doi.org/10.5281/zenodo.7576163.
(65) Friedrich, C.; Blügel, S.; Schindlmayr, A. Efficient Implementation of the *GW* Approximation within the All-Electron FLAPW Method. *Phys. Rev. B* **2010**, *81*, No. 125102.
(66) Friedrich, C.; Blügel, S.; Schindlmayr, A. Erratum: Efficient Implementation of the *GW* Approximation within the All-Electron FLAPW Method [Phys. Rev. B 81, 125102 (2010)]. *Phys. Rev. B* **2021**, *104*, No. 039901.
(67) Adler, S. L. Quantum Theory of the Dielectric Constant in Real Solids. *Phys. Rev.* **1962**, *126*, 413−420.
(68) Wiser, N. Dielectric Constant with Local Field Effects Included. *Phys. Rev.* **1963**, *129*, 62−69.
(69) Rubel, O.; Bokhanchuk, A.; Ahmed, S. J.; Assmann, E. Unfolding the Band Structure of Disordered Solids: From Bound States to High-Mobility Kane Fermions. *Phys. Rev. B* **2014**, *90*, No. 115202.
(70) Andersen, O. K. Linear Methods in Band Theory. *Phys. Rev. B* **1975**, *12*, 3060−3083.
(71) Tonndorf, P.; Schmidt, R.; Böttger, P.; Zhang, X.; Börner, J.; Liebig, A.; Albrecht, M.; Kloc, C.; Gordan, O.; Zahn, D. R. T.; de Vasconcellos, S. M. Bratschitsch, R. Photoluminescence Emission and Raman Response of Monolayer MoS_2, $MoSe_2$, and WSe_2. *Opt. Express* **2013**, *21*, 4908−4916.
(72) Albrecht, W.; Moers, J.; Hermanns, B. HNF - Helmholtz Nano Facility. *J. Large-Scale Res. Facil. JLSRF* **2017**, *3*, No. A112.
(73) Momma, K.; Izumi, F. *VESTA3* for Three-Dimensional Visualization of Crystal, Volumetric and Morphology Data. *J. Appl. Crystallogr.* **2011**, *44*, 1272−1276.

https://doi.org/10.1021/acsami.3c05366
ACS Appl. Mater. Interfaces 2023, 15, 35321−35331